PAPER

Pristine conductive metal–organic framework film as a cost-effective counter electrode for dye-sensitized solar cells

Alisha Gogia,[a] Navdeep Kaur,[a] Cheng-Yu Lai[ab] and Daniela Radu (iD) *[a]

The development of cost-effective and efficient alternatives to platinum (Pt) counter electrodes (CE) is critical for advancing dye-sensitized solar cells towards scalable and affordable applications. Here, we demonstrate the use of pristine, two-dimensional, conductive copper-benzenehexathiol metal–organic framework, CuBHT MOF, with a kagome lattice, as a Pt-free CE. Unlike conventional approaches that rely on MOF-derived metal-oxides or carbon composites, we utilize CuBHT in its unmodified form, leveraging its high electrical conductivity and π–d conjugation. Uniform CuBHT thin film was fabricated on fluorine-doped tin oxide substrates *via* the interfacial growth method. Structural and chemical analysis (powder X-ray diffraction analysis, Raman, and X-ray photoelectron spectroscopy) confirmed that the films retain the crystallinity and composition of bulk CuBHT powder, while scanning electron microscopy and atomic force microscopy demonstrated the formation of continuous films. Cyclic voltammetry revealed excellent electrocatalytic activity of CuBHT thin film towards both I_3^-/I^- and I_2/I^- redox couples, comparable to Pt CE. Photovoltaic measurements and electrochemical impedance spectroscopy further demonstrated effective charge transfer and catalytic behavior, yielding a peak power conversion efficiency of 6.27 ± 0.02% surpassing that of Pt CEs (5.99 ± 0.01%) in reference devices. These findings establish CuBHT as a promising Pt-free CE for next-generation DSSCs.

Introduction

Dye-sensitized solar cells (DSSCs) offer a modular and cost-effective alternative to traditional photovoltaic devices, owing to their unique architecture that decouples light absorption, charge separation, and charge transport into different materials, allowing independent modulation of each function.[1] A standard DSSC consists of a dye-sensitized photoanode, a redox electrolyte, and a counter electrode (CE) that facilitates the regeneration of the redox mediator. During operation, the photoexcited electrons from the dye are injected into the conduction band of the semiconductor (TiO$_2$ coated on fluorine-doped tin oxide (FTO) glass), from where they are transported through the external circuit to the CE (typically Pt). Meanwhile, the oxidized dye molecules are regenerated by iodide ions (I$^-$) in the electrolyte, forming triiodide.[2] The CE is responsible for reducing I$_3^-$ back to I$^-$ by catalyzing its reaction with the incoming electrons, thereby regenerating the redox mediator and closing the circuit.

Various efforts have been made to improve each aspect of DSSCs; for example, with respect to the dyes, various π-extended porphyrins and anthracene-bridged dyes have been developed for visible-NIR absorption to enhance light harvesting,[3,4] twisted phenothiazine molecules have been designed for tuned HOMO–LUMO alignment and aggregation suppression,[5] and donor-π-acceptor architectures have been used that optimize both charge injection and stability.[6,7] At the photoanode level, modifications such as metal-ion doping (*e.g.*, Fe/S),[8] morphological control (nanotubes, nanowires),[9] and light scattering composites[10,11] have been employed to enhance dye uptake, narrow TiO$_2$ band gap, boost charge transport, and reduce recombination losses. While substantial progress has been made in optimizing photoanodes and sensitizers, the counter electrode (CE) remains a critical bottleneck, traditionally relying on platinum due to its exceptional catalytic performance. While Pt offers outstanding catalytic performance, its high cost, scarcity, and susceptibility to corrosion present serious limitations for large-scale, economically viable deployment. These drawbacks motivate the search for alternative CE materials that are not only catalytically active but also processable, scalable, and stable. To serve as an effective CE material, the materials should (i) have high electrical conductivity to ensure efficient

[a] Department of Mechanical and Materials Engineering, Florida International University, Miami, Florida 33174, USA
[b] Department of Chemistry and Biochemistry, Florida International University, Miami, Florida 33199, USA. E-mail: dradu@fiu.edu

electron transfer from the external circuit to the electrolyte, (ii) exhibit strong electrocatalytic activity towards the reduction of the I_3^-/I^- redox couple, (iii) have good adhesion with the substrate to form stable and uniform films, and (iv) be cost-effective.[12]

To address these issues, alternative materials such as carbon-based composites,[13,14] transition metal sulfides,[15] metal oxides,[16,17] and conductive polymer composites[18,19] have been explored. More recently, metal–organic frameworks (MOFs) have attracted attention for a wide variety of applications.[20,21] MOFs are a class of crystalline hybrid organic–inorganic materials composed of metal ions or clusters coordinated to organic ligands, forming porous structures.[22,23] Their modular design allows for precise control of porosity, surface area, and functionality, making them useful for different applications ranging from gas storage and sensing to catalysis and energy devices.[24] However, the poor electrical conductivity of most MOFs has limited their role in DSSCs to the photoanode or as precursors to conductive derivatives such as metal oxides or carbon routes that add complexity and cost.[25–30] The poor electrical conductivity of MOFs restricts their ability to support efficient charge transfer, thereby hindering their catalytic performance at the CE/electrolyte interface.[31,32] As a result, the use of pristine MOFs as CEs has remained rare and largely unexplored.

In this work, we address this challenge by employing a pristine two-dimensional π–d conjugated conductive copper benzenehexathiol (CuBHT) MOF, as a counter electrode material in its pristine form offering cheaper and scalable alternative to platinum counter electrodes in DSSCs. CuBHT is a highly crystalline two-dimensional MOF with a kagome lattice, first reported by Huang *et al.* in 2015, exhibiting excellent conductivity (1580 S cm^{-1}) attributed to strong π–d conjugation and electron delocalization in the 2D framework.[33] Since then, CuBHT MOF has been utilized in different applied fields like lithium-ion batteries,[34,35] sensing,[36,37] and hydrogen evolution catalysts.[38] Jin *et al.* introduced CuBHT layer as an alternative to transparent conductive oxide in perovskite solar cells, PbS quantum dots solar cells, and PTBZ:PCBM organic solar cells, and the device performance was found to be comparable to the widely used ITO electrode.[39] Chen *et al.* demonstrated the ultrafast *in situ* growth of high-quality, uniform, and large-area CuBHT MOF thin films with excellent conductivity and substrate adhesion for their use in flexible electronic devices.[36] Huang *et al.* further demonstrated the use of morphology-controlled CuBHT MOF for enhanced electrocatalytic activity in the hydrogen evolution reaction.[38] Wu *et al.* demonstrated that ultrathin CuBHT films can maintain high conductivity and long-term stability on flexible substrates.[40] Inspired by these studies, we chose to use CuBHT as an alternative to Pt counter electrode in DSSCs. Unlike previous studies that employed various MOF-derived metal oxides as Pt-free CEs, we have used a MOF in its pristine form as a Pt-free CE. The purity of the obtained thin film is confirmed by a comparison of powder X-ray diffraction (PXRD) analysis and Raman spectroscopy study with the bulk CuBHT powder sample. Scanning electron microscopy (SEM) and atomic-force microscopy (AFM) measurements are used to verify the film quality, and the conductivity measurements were done through four-probe measurements. The device efficiency was evaluated by measuring photovoltaic (PV) performance, analyzing charge transport characteristics through electrochemical impedance spectroscopy (EIS), and correlating them with electrocatalytic performance observed from cyclic voltammetry (CV) and conductivity measurement.

Experimental

Materials

Copper(II) nitrate trihydrate ($Cu(NO_3)_2 \cdot 3H_2O$, 99%, for analysis) was purchased from Acros Organics. Benzenehexathiol (BHT, 98%) was purchased from Ambeed. Hydrogen peroxide (H_2O_2, ACS grade, 30%), chlorobenzene (99%), sodium bromide (NaBr), and potassium hydroxide (KOH) were purchased from Thermo Fischer Scientific. Nanopure water and chlorobenzene were degassed with the freeze–thaw method using a Schlenk line and liquid nitrogen before using them for synthesis. Thin films of CuBHT MOF were prepared on glass substrates with fluorine-doped tin oxide (FTO) coating. Materials used in the fabrication of the device included FTO substrates obtained from Hartford Glass Co., Inc. Reagents such as zinc powder, titanium(IV) isopropoxide (TTIP), mesoporous titanium dioxide (m-TiO$_2$) paste with an average particle size of ∼20 mm, lithium iodide (LiI), lithium perchlorate (LiClO$_4$), and iodine (I$_2$) were purchased from Sigma-Aldrich (Saint Louis, MI). Hydrochloric acid (HCl) was purchased from Thermo Fischer Scientific. Platisol-T was sourced from Solaronix (Aubonne, Switzerland), N719 dye (ditetrabutylammonium *cis*-bis(isothiocyanato)bis-(2,2′-bipyridyl-4,4′-dicarboxato)ruthenium(II)) and EL-HSE electrolyte were supplied by Greatcell Solar Co. Ltd. (Queanbeyan, Australia). All the chemicals were used as-obtained without further purification unless specified.

Characterization

Powder X-ray diffraction (PXRD) analysis was carried out using a Rigaku MiniFlex system equipped with a Cu-Kα radiation source (λ = 1.5405 Å), operating at 40 mV and 30 mA. Raman spectra were recorded on a WITec α300 Raman microscope utilizing a 532 nm laser. Scanning electron microscope (SEM) images were collected using a JEOL/JSM-F100 Schottky field emission SEM equipped with an energy-dispersive X-ray spectroscopy detector (SEM/EDX). AFM images were obtained on an Anton Paar Tosca 400 AFM. CV measurements were performed using the same instrument, employing a three-electrode system. The three-electrode system included a Pt counter electrode, a Ag/AgCl reference electrode, and the target sample (Pt or CuBHT films) on the FTO substrate as the working electrode. All three electrodes were immersed in an electrolyte containing LiClO$_4$ (0.1 M), I$_2$

© 2026 The Author(s). Published by the Royal Society of Chemistry

RSC Appl. Interfaces, 2026, **3**, 420–430 | 421

(1 mM), and LiI (10 mM) in an acetonitrile solution at room temperature. CV data for the Pt and CuBHT films on FTO were collected within the voltage range of −1 to 1 V, starting and stopping potential at 0 V, and a scan rate of 50 mV s^{-1}. A stabilization time of 5 s was maintained before recording the CV data. Electrical conductivity was measured by using an Ossila T2001A3 four-point probe station by fabricating CuBHT films using the same process on glass to avoid interference from FTO. PV cell testing was performed with an ORIEL LCS-100TM solar simulator under one sun illumination (1.5 G AM) at an incident power intensity of 100 mW cm^{-2}. Transmission electron microscopy (TEM) samples were prepared by dropping dilute dispersions of each nanoparticle batch onto Au TEM grids. High-resolution TEM (HR-TEM) images were obtained on JEOL JEM-2100 Plus with a 200 kV LaB6 electron source. The solar simulator was calibrated with a silicon solar cell for data accuracy. XPS measurements of CuBHT film and powder were conducted using a Thermo Fisher Scientific Nexsa spectrometer equipped with a monochromatic Al Kα X-ray source (hv = 1486.6 eV). Data were collected with a 400 μm spot size. The spectrometer was energy calibrated using the adventitious carbon C 1s peak at 284.8 eV. Wide-scan survey spectra were recorded over the 0–1200 eV binding energy range with a pass energy of 100 eV, while high-resolution scans of Cu 2p, S 2p, and C 1s regions were acquired at a pass energy of 50 eV. Spectral deconvolution was carried out using Thermo Fisher Avantage software, employing a mixed Gaussian–Lorentzian (70 : 30) fitting function. Signal optimization ensured reliable identification and quantification of elemental states. X-ray fluorescence (XRF) spectra were collected using an ATLAS instrument (IXRF Systems, USA) to determine the elemental composition of the film. EIS measurements of the fabricated DSSCs were performed immediately after the J–V measurements using an Ω Metrohm Autolab instrument. The measurements were conducted by connecting the FTO part of the photoanode and CE to the Autolab instrument using a two-electrode electrochemical setup. The measurements were conducted for all fabricated DSSCs under standard one-sun illumination (100 mW cm^{-2}), spanning a frequency range of 0.1 Hz to 1 MHz, at the open-circuit voltage (V_{OC}) determined from the J–V curves of each device.

Cleaning and activation of FTO glass substrates

The FTO glass substrates were first cleaned by sequentially ultrasonicating them in water, acetone, ethanol, and isopropyl alcohol for 5 min each, followed by drying in an oven and flushing with nitrogen to dry off any solvent. This was followed by an additional step of ozone treatment for 20 min. The substrates were then activated by an additional hydroxylation step by treating with a mixture of hydrogen peroxide (30%) and KOH (2 mmol) aqueous solution at a volume ratio of 1 : 3 for 30 min at 80 °C. After this, the substrates were rinsed with water and ethanol, and dried under nitrogen flux for the next step.

Preparation of solutions

The FTO glass substrates were first cleaned by sequentially ultrasonicating Both solvents, nanopure water and chlorobenzene, were degassed using a Schlenk line by the freeze–thaw method. Under argon atmosphere, BHT (0.5 mM, 2.6 mg) was dissolved in 20 mL degassed chlorobenzene, and Cu(NO$_3$)$_2$·3H$_2$O (5 mM, 24.2 mg) and NaBr (1 mM, 2.05 mg) were dissolved in 20 mL degassed water. These flasks were sealed and used later for the fabrication of thin CuBHT MOF films.

Fabrication of CuBHT MOF film

A thin film of CuBHT MOF was obtained on an activated FTO substrate by liquid–liquid interfacial reaction between a very thin layer of organic BHT layer and aq. Cu(NO$_3$)$_2$/NaBr on a spin coater.[36] The hydroxyl-activated FTO substrate was covered on one edge with Kapton tape and placed on a spin coater to fabricate CuBHT CE. In a typical process, 600 μL of the previously prepared Cu(NO$_3$)$_2$·3H$_2$O/NaBr (5 mM/1 mM) was dropped on the prepared FTO substrate, let to sit for 5 min, and then the spin coater was started at 500 rpm for 20 s to get a thin layer of metal salt on the FTO surface. The idea was not to let the layer completely dry off. To this, 200 μL of previously prepared BHT solution was dropped, which covered the entire surface of FTO. This was left to stay for different time intervals and then spun in a two-step process (first at 500 rpm for 10 s and then at 1500 rpm for 45 s to completely dry off the excess solvents) to get an extremely thin and uniform layer of CuBHT MOF film, formed by the interfacial liquid–liquid reaction between the metal salt and the ligand. The film was washed with chlorobenzene and ethanol and dried under vacuum for 12 h for further characterization and application.

Synthesis of bulk powder of CuBHT MOF

In a typical reaction, 0.1 mmol (27 mg) of BHT was dissolved in 100 mL of chlorobenzene and transferred to a 250 mL dried, degassed flask, purged with inert gas, forming layer 1. Over this, 50 mL degassed water layer was slowly added from the sides of the flask, which acted as a buffer layer. Subsequently, layer 2, consisting of 60 mL aq. solution containing 0.3 mmol (72 mg) of Cu(NO$_3$)$_2$·3H$_2$O and 0.06 mmol (6.2 mg) of NaBr was introduced over the buffer layer. A blue shiny layer started to develop within minutes of introducing layer 2. The setup was left undisturbed for 7 days to get the maximum yield of CuBHT MOF powder. The interfacial film was filtered using a Buchner funnel to isolate the powder, washed sequentially with ethanol and acetone, and dried under vacuum at 60 °C for 30 minutes.

DSSC device fabrication

DSSCs were assembled following protocols established in our previous studies.[11,41,42] Photoanodes and counter electrodes (CEs) were prepared separately and sandwiched together

using a cellulose acetate spacer, with 60 μL of $I^-/I_3^-/$ electrolyte added between them.

Photoanode preparation. Patterned FTO substrates were chemically etched using zinc paste and aqueous 6 M HCl (18.5% v/v), then thoroughly cleaned by sequential ultrasonication in Hellmanex cleaning solution, water, acetone, ethanol, and isopropanol at 80 °C. Between each washing step, the substrates were dried under a nitrogen flow. After drying under nitrogen, substrates were treated with UV-ozone (30 min) and subsequently heated at 450 °C. Once the temperature was reached, a compact TiO_2 (c-TiO_2) layer was spray-coated using a 0.4 M TTIP solution in ethanol, let it sit for 30 min, and cooled to room temperature. This was followed by doctor-blading an m-TiO_2 layer (0.15 cm^2 active area). The m-TiO_2/c-TiO_2/FTO substrate was annealed at 450 °C for 1 h, yielding an m-TiO_2 thickness of ~11.5 μm (SEM), as reported in our previous work.[44] Finally, the substrates were soaked in 0.4 mM N719 dye (ethanol) for 20 h.

Reference counter electrode preparation. Pt reference CEs were fabricated by drop-casting 60 μL of Platisol-T onto cleaned FTO and annealing at 450 °C for 30 min. CuBHT-based CEs were fabricated using MOF film as detailed previously.

Results and discussion

Synthesis and characterization

A thin film of CuBHT MOF was synthesized on FTO substrates as a potential alternative to conventional Pt counter electrodes used in DSSCs. A schematic representation of the thin-film fabrication process is shown in Scheme 1. The interfacial method involves a liquid–liquid interfacial reaction between an aqueous phase containing Cu^{2+}/Br^- salt and an organic phase containing the BHT ligand dissolved in chlorobenzene. The role of NaBr is to support the formation of a uniform film by acting as a coordination modulator, suppressing nucleation, while also stabilizing the mixed Cu^{2+}/Cu^+ environment of CuBHT MOF.[33] The MOF film forms at the interface through diffusion of metal ions and ligands across the solvent boundary, and its thickness increases with reaction time.[36]

In Pt-free DSSCs, a uniform and high-quality film with a large contact area is important to have efficient electrochemical reactions at the CE. To evaluate the morphology, composition, and thickness of the fabricated CuBHT films on FTO, SEM, EDX, and AFM imaging were used. The top-view SEM of the film (Fig. 1(a)) revealed a continuous and uniform film consisting of tiny, closely packed, crystal particles with numerous grain boundaries. This compact arrangement is advantageous for maximizing the electrochemically active surface area and ensuring efficient charge transfer at the counter electrode/electrolyte interface in DSSCs. AFM further confirmed the uniformity of the films, with a root mean square (RMS) roughness of only ~15 nm over a scan area of 5 × 5 μm (Fig. 1(b)). The thickness of CuBHT film was determined through cross-sectional SEM (Fig. 1(c)), which shows ~500 nm FTO layer and the ~520 nm CuBHT layer. EDX scan across the cross section differentiates the elements of the underlying FTO (Sn, O) and the CuBHT layer (Cu, C, and S), verifying film uniform deposition (Fig. 1(d)). UV/vis spectra in the 400–800 nm region of the CuBHT/FTO electrode show transmittance increasing from ~42% at 400 nm to a maximum of ~68% around 520–540 nm (Fig. S1). The broadband attenuation in the blue region is consistent with π–π* transitions and metal–ligand charge transfer absorption in conjugated 2D MOFs. A transmittance of 50–70% of the film across the visible range confirms its suitability for semi-transparent DSSCs. The electrical conductivity of the pristine CuBHT film deposited on glass was measured using a four-probe method and exhibited a conductivity of ~97 S cm^{-1}, which reflects its strong π–d conjugation and extended electron delocalization within the kagome lattice.

Since CuBHT films in this work are very thin, conventional powder-based structural analyses such as PXRD could not be directly performed on the films due to the low scattering volume. To validate the structural identity of the films, we
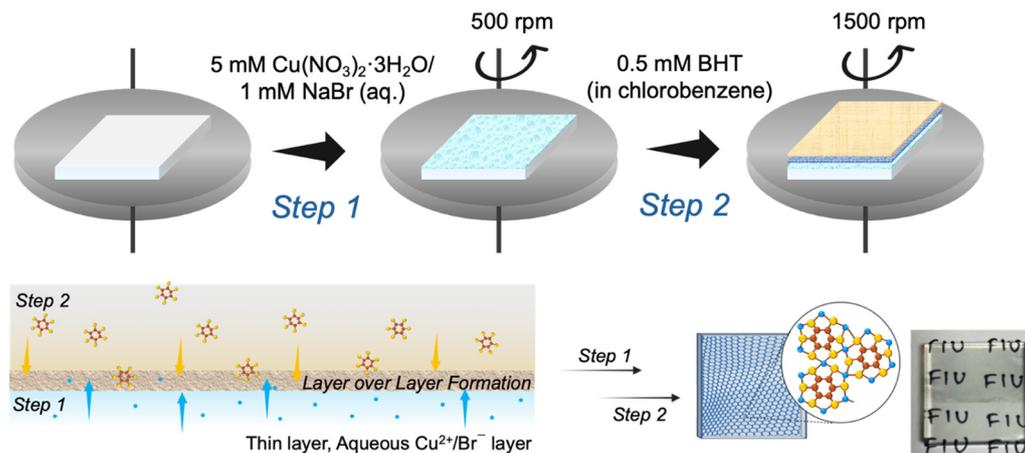
Scheme 1 Schematic representation of CuBHT film fabrication *via* the interfacial liquid–liquid deposition method.
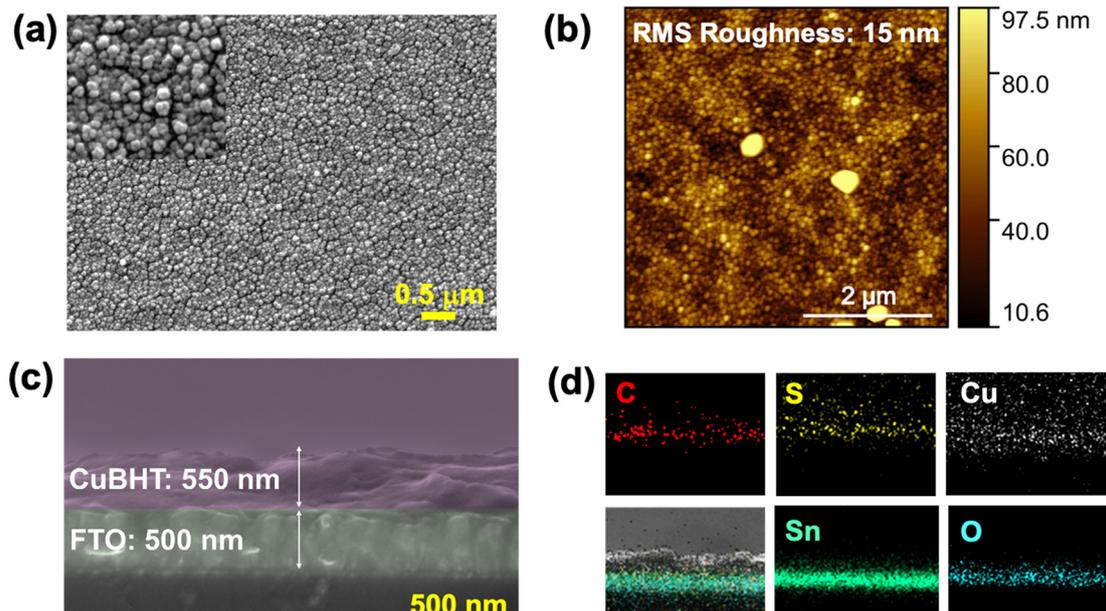
Fig. 1 Surface analysis of CuBHT film on FTO substrate: (a) top-view SEM, (b) AFM topography, (c) cross-sectional SEM, and (d) cross-sectional SEM–EDX mapping images.

compared the PXRD with that of bulk CuBHT powder. The bulk powder was synthesized by replicating the interfacial reaction between aq. $Cu(NO_3)_2$/NaBr and organic BHT layers at higher concentrations to enable isolation of sufficient material for detailed characterization.[43] This reaction at the interface initiates rapidly, resembling the thin film deposition process, and was progressed over 7 days to yield the maximum amount of CuBHT MOF powder (Fig. S2). A schematic of the chemical

reaction and the structure of CuBHT MOF is shown in Fig. 2(a). The PXRD pattern (Fig. 2(b)) of the synthesized CuBHT bulk powder exhibited the expected reflections for a crystalline 2D CuBHT framework, including the intense (100) and (001) peaks at $2\theta \sim 13°$, $27°$, corresponding to in-plane periodicity of the kagome lattice and $\pi–\pi$ stacking interactions in the layered MOF.[38,43] The peaks at higher angles also match with the monoclinic $P2_1/c$ unit cell parameters ($a = 14.81$ Å, $b = 8.67$ Å,
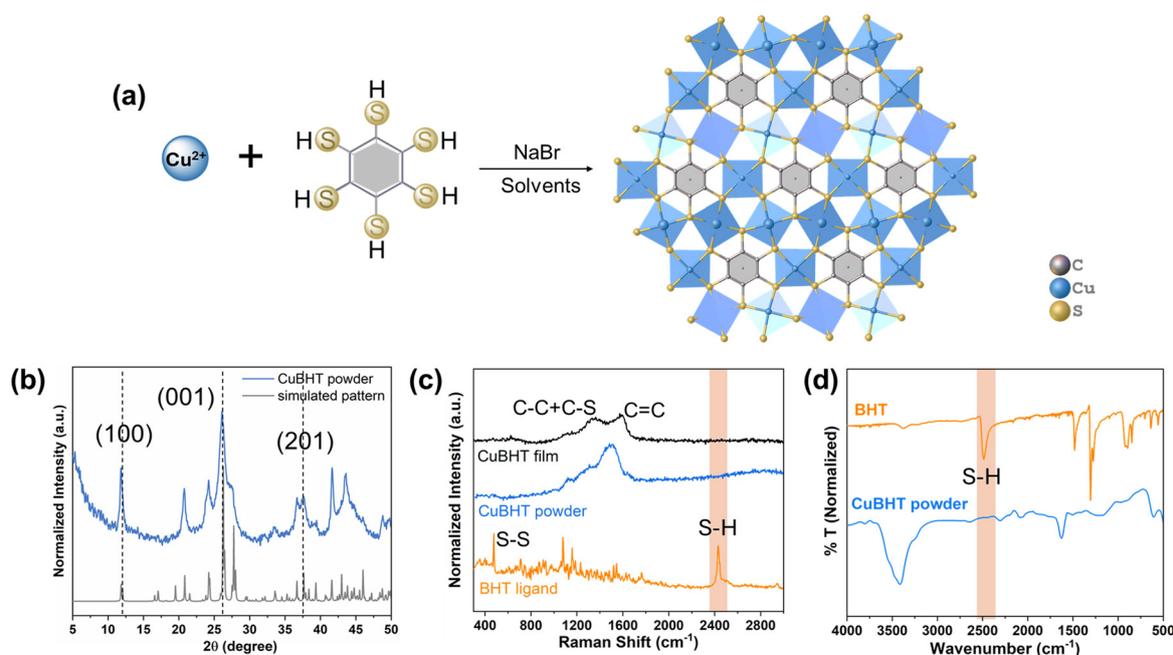

Fig. 2 (a) Schematic of the chemical reaction for the formation of CuBHT MOF of synthesized CuBHT MOF; crystal structure visualized using previously reported CIF data (ref. 43, CCDC 2381830), (b) PXRD profile of bulk CuBHT powder and its simulated pattern, (c) Raman spectra of BHT, CuBHT bulk powder, and CuBHT film, and (d) FTIR spectra of BHT and CuBHT bulk powder.

c = 6.84 Å, β = 97.34°) refined from synchrotron diffraction in the reference structure.[43] While thin-film PXRD was limited by signal intensity, Raman and XPS measurements allowed a direct comparison between the bulk and thin-film forms. Fig. 2(c) shows the Raman spectra of CuBHT bulk powder, pure BHT ligand, and CuBHT thin film on FTO. CuBHT powder spectrum displays a broad set of vibrational bands in the region of 1024 and 1700 cm^{-1}, consistent with the vibrational bands for Cu–S coordination frameworks. In contrast to the free BHT ligand, which displays a sharp peak at 2495 cm^{-1}, this band is entirely absent in the case of both CuBHT MOF powder and films, confirming complete deprotonation of S–H bonds upon coordination with the copper ions in the framework. The CuBHT films and powder features closely align with the vibration features of highly ordered single crystals and previously fabricated thin films of CuBHT MOF.[34,40,43] Slight shifts between the Raman spectra of the powder and thin film were observed, likely arising from substrate-induced effects, a common feature when comparing powders with thin films.[44] Further, comparison of the FTIR spectra of the BHT ligand and CuBHT MOF powder revealed the absence of a peak at ~2490 cm^{-1} corresponding to the thiol group, proving the successful formation of MOF (Fig. 2(d)).

The dark-blue flaky CuBHT material obtained from bulk powder was ground into a fine powder for TEM analysis. Fig. 3(a) and (b) show the photograph and SEM images of the bulk material before and after grinding. The HRTEM image of the material reveals lattice fringes with a spacing of ~3.5 Å, which can be assigned to the (001) plane of the monoclinic CuBHT structure. This matches well with the PXRD peak observed at 2θ = 27°, corresponding to a d-spacing of ~3.3 Å (Fig. 3(c) and (d)).

XPS analyses of the CuBHT bulk powder and thin film were performed to get an insight into the elemental composition and their chemical states. Fig. 4(a) displays the XPS survey spectra of CuBHT powder and thin film on FTO collected over a range of 0 to 1200 eV, confirming their similarity and successful formation of the CuBHT framework.[40] The survey scans of both CuBHT powder and film show the presence of Cu, S, and C from the MOF framework along with oxygen from the air exposure, and Sn from the conductive FTO substrate used for XPS analysis (Fig. 4(a)). The high-resolution spectrum corresponding to the narrow scan of Cu 2p ranging from 960 to 928 eV consists of two spin–orbit peaks corresponding to Cu 2p$_{3/2}$ and Cu 2p$_{1/2}$ centered at 932.17 eV and 952.3 eV, respectively (Fig. 4(b)). The asymmetry in the peaks suggests that there are two kinds of copper with different oxidation states (Cu^{2+}/Cu^{+}). The Cu 2p$_{3/2}$ is deconvoluted into two subpeaks centered at 932.2 eV and 933.9 eV corresponding to Cu^{+} and Cu^{2+}, respectively. Similarly, the Cu 2p$_{1/2}$ is deconvoluted into two subpeaks centered at 951.9 eV and 953.9 eV corresponding to Cu^{+} and Cu^{2+}, respectively.

Quantitative analysis based on the peak areas indicates that Cu^{+} is the dominant oxidation state, accounting for ~57.3 atomic% of the total copper, while Cu^{2+} contributes ~42.7 atomic%. The resulting Cu^{+}:Cu^{2+} atomic percentage ratio, calculated from the fitted peak areas, is approximately 1.34:1. The detailed fitting parameters and area-based calculations are provided in Table S1. The coexistence of Cu^{2+} and Cu^{+} is also marked by the presence of characteristic satellite peaks for Cu^{2+}, between 940–950 eV, indicating its d^9 configuration and associated shake-up transitions.[45,46] The narrow scan of S 2p region spanning between the binding energy range of 172 eV to 160 eV consists of a broad asymmetric peak between 166 eV and 161 eV showing two merged doublets corresponding to S 2p$_{1/2}$ and S 2p$_{3/2}$ orbit peaks of S–Cu and S–C bonds (Fig. 4(c)). These peaks lie in the region of typical thiolate bonding, confirming the coordination of thiol groups with copper ions in CuBHT MOF.[40] The deconvoluted subpeaks centered at 161.8 eV and 163.4 eV correspond to the S 2p$_{3/2}$ and S 2p$_{1/2}$ spin–orbits of S–C bond, while the subpeaks at 163.2 eV and 164.5 eV correspond to the S 2p$_{3/2}$ and S 2p$_{1/2}$ spin–orbits of S–Cu bond, respectively. Another broad peak ranging from 172 to 166 eV is observed, which may correspond to the oxidation of surface-exposed sulfur atoms on the top layer of film. The C 1s narrow scan indicates the aromatic carbon environment of the benzene rings in the BHT ligand with a dominant peak centered at 284.7 eV (Fig. 4(d)). A deconvoluted subpeak at 285.8 eV is attributed to the C–S bonding, indicating the coordination of thiol groups to copper centers. Minor contributions at higher binding energies (~287.7 eV) can be assigned to the oxidized carbon species, likely due to surface exposure or residual solvent impurities. XPS of the bulk phase powder sample drop-casted on FTO substrate also shows similar XPS survey spectra and narrow scans of the C 1s, Cu 2p, and S 2p regions (Fig. S3). The XRF spectrum showed clear signals for Cu and S, consistent with the expected Cu:S ratio of ~1:2 for CuBHT. Carbon was not
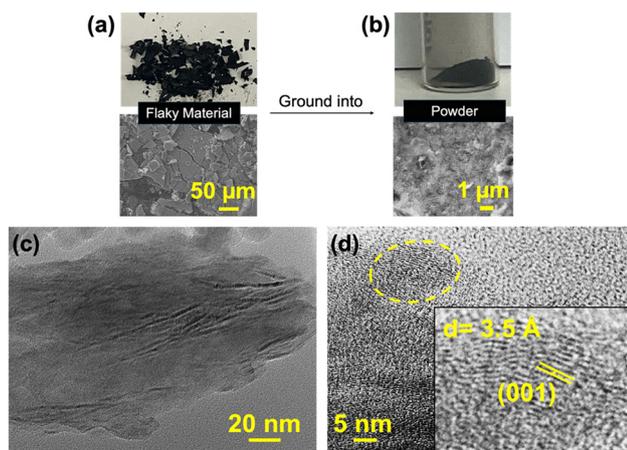

Fig. 3 (a and b) Photographs and SEM images showing the initial flake-like material formed in the interfacial synthesis reaction of bulk CuBHT MOF powder and its corresponding powder after crushing, and (c and d) HRTEM images of CuBHT MOF powder; the inset is a high-resolution image to depict the lattice plane and d-spacing.

© 2026 The Author(s). Published by the Royal Society of Chemistry

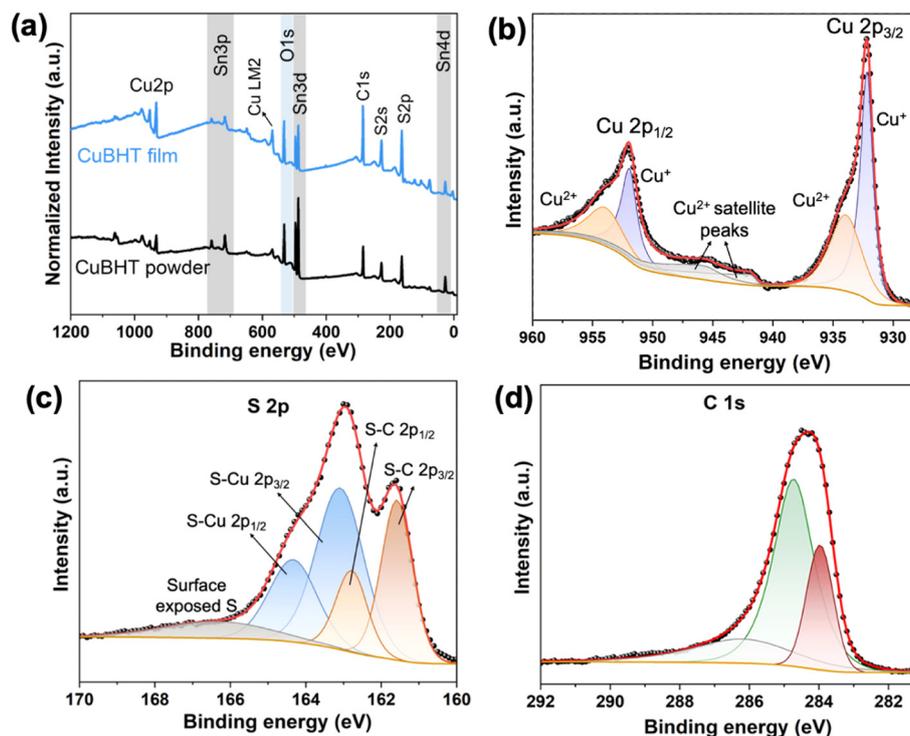*RSC Appl. Interfaces*, 2026, **3**, 420–430 | **425**

Fig. 4 (a) XPS survey spectra of CuBHT film and bulk powder, high-resolution narrow scans of the CuBHT film for (b) Cu 2p, (c) S 2p, and (d) C 1s regions.

observed due to the poor sensitivity of XRF detector toward light elements (Fig. S4).

Cyclic voltammetry measurements

The electrocatalytic activity of a material is a key parameter in analysing its suitability as a CE in DSSCs, in addition to its conductivity. The process involves immersing the fabricated film in an electrolyte and assessing its electrochemical behaviour using cyclic voltammetry in a standard three-electrode set-up.[11,41,42] This system consisted of an Ag/AgCl reference electrode, a Pt wire as the counter electrode, and

CuBHT thin film and Pt thin films as working electrodes. The electrolyte solution contained 0.1 M $LiClO_4$, 1 mM I_2, and 10 mM LiI dissolved in acetonitrile. The electrocatalytic performance of each CE was evaluated based on two primary parameters: (i) the cathodic (reduction) peak current density (J_{PC}), and (ii) peak-to-peak separation (ΔE_{pp}) in reduction peaks. A high J_{PC} and combined with a low ΔE_{pp} reflects efficient catalytic activity. As expected, Pt electrode displays two pairs of oxidation and reduction peaks (Fig. 5(a)), corresponding to the two redox reactions enabled by Pt:
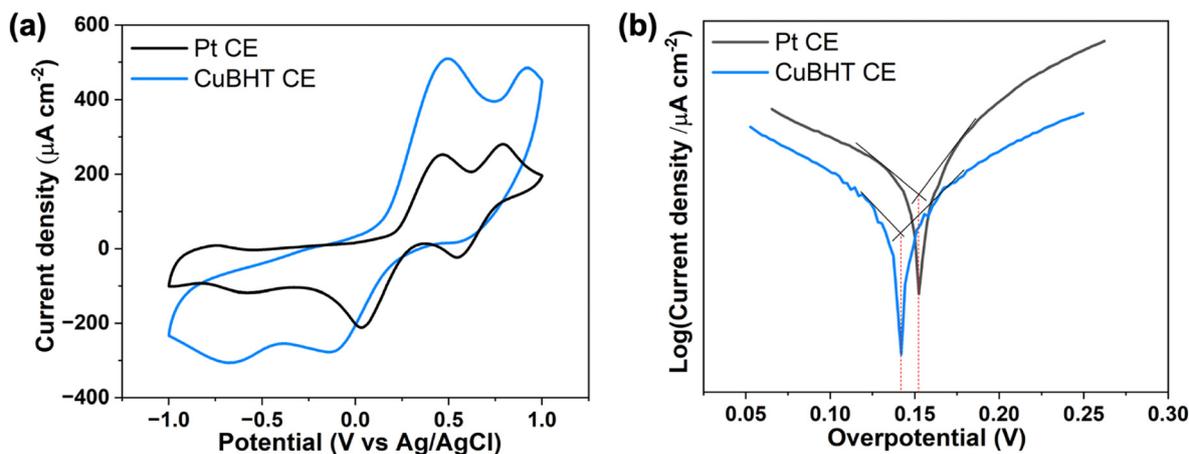
$$I_3^- + 2e^- \rightarrow 3I^- \tag{1}$$

Fig. 5 (a) Cyclic voltammetry curves and (b) Tafel plots of reference Pt and CuBHT CEs.

$$I_2 + 2e^- \rightarrow 2I^- \qquad (2)$$

Interestingly, the CV of the CuBHT film also revealed two distinct pairs of oxidation and reduction peaks, similar to the Pt counter electrode. Pt electrode is known for its exceptional catalytic activity of efficiently catalyzing both the redox reactions, resulting in two well-defined peaks (Fig. 5(a)). The observation of similar behaviour in the case of CuBHT highlights its efficiency to catalyse not just the primary I_3^-/I^- redox couple but also the additional reduction of molecular iodine to iodide/polyiodide species. This behaviour indicates that the CuBHT film facilitating a multi-step charge transfer process is comparable to Pt CE and highlights that CuBHT can also act as an effective and versatile electrocatalyst for iodine regeneration in DSSCs. The CuBHT film exhibited a significantly higher cathodic peak current density (J_{PC} = 277 µA cm^2) compared to the Pt counter electrode (J_{PC} = 210 µA cm^2). Additionally, the reduction peak appeared at a more negative potential, resulting in a larger peak-to-peak separation (ΔE_{PP}). The higher J_{PC} may be attributed to the strong electrocatalytic activity owing to the good film conductivity and efficient Cu–S catalytic sites. However, the larger ΔE_{PP} suggests comparatively slower charge transfer kinetics, possibly due to surface heterogeneity causing less efficient charge transport at the electrode–electrolyte interface. Fig. 5(b) shows the Tafel polarization plots of CuBHT thin film CE with respect to the Pt CE. As shown in the Tafel plots, both CuBHT thin film and Pt exhibit well-defined anodic and cathodic branches, characteristic of efficient catalytic behaviour. The extrapolated overpotential of CuBHT CE (0.14 V) exhibits a marginal difference compared to the standard Pt CE (0.15 V), highlighting its comparable catalytic efficiency with that of Pt CE. These results confirm that CuBHT CE can effectively facilitate I_3^-/I^- reduction at the CE/electrolyte interface and serve as a promising Pt-free alternative in DSSCs. Finally, a detailed study of the photovoltaic performance of the CuBHT film was done, as discussed in the following section.

Photovoltaic performance of CuBHT film as CEs

To evaluate the effectiveness of CuBHT film as an alternative to Pt CEs in DSSCs, J–V characteristics of DSSCs with reference Pt CE were obtained under 1 sun illumination with light power intensity of 100 mW cm^{-2} (AM 1.5 G). The performance was evaluated by the following photovoltaic (PV) parameters: (i) short-circuit current density (J_{SC}), (ii) open-circuit voltage (V_{OC}), (iii) fill-factor (FF), (iv) power conversion efficiency (PCE).

To establish optimal conditions for employing CuBHT MOF film as CE in DSSCs, we standardized the effect of the contact time of BHT on the device performance, with 5 mM Cu(NO$_3$)$_2$ salt solution, 1 mM NaBr, and 0.5 mM of BHT. Specifically, we varied the duration for which BHT ligand was allowed to interact with the Cu^{2+}/Br$^-$ layer for 2 min, 5 min, and 8 min. The corresponding PV performance results are

summarized in Table S2, including a control device using just pristine FTO glass as the CE. Fig. S5 shows the J–V curves, Nyquist plots, and Bode plots for devices corresponding to these optimizations with respect to the reference Pt electrode. The optimal conditions for the best device performance were found to be: interfacial reaction involving 5 mM Cu(NO$_3$)$_2$/1 mM NaBr aq. solutions and 0.5 mM BHT chlorobenzene solution with a 5 min reaction time. Using these conditions, reproducible and consistent results were obtained for multiple devices, indicating the robustness of both the fabrication techniques and device performances (error bars are included in Table 1 for 5 devices each fabricated under similar experimental conditions). Fig. 6(a) shows the photocurrent density–voltage (J–V) of the optimized DSSCs with CuBHT CE with a reference Pt. The device with optimized conditions for CuBHT CE shows a PCE of 6.27%, which is more than that of Pt CE (Table 1).

Other key performing parameters, such as J_{SC}, V_{OC}, and FF, are also either comparable or superior in CuBHT-based devices (J_{SC} = 12.11 mA cm^{-2}, V_{OC} = 0.74 V, and FF = 0.69) than the Pt CE (J_{SC} = 11.59 mA cm^{-2}, V_{OC} = 0.74 V, and FF = 0.69). This could be attributed to the good conductivity of CuBHT MOF, which facilitates electron transfer, and the uniform film formation provides continuous and direct transfer pathways, reducing resistance.

To further study the enhanced charge collection and improved PCE in CuBHT-based devices, the external quantum efficiency (EQE) spectra were measured (Fig. 6(b)). EQE is a measure of the conversion of incident photons into charge carriers and is mathematically described by eqn (S1). In the visible wavelength range of 400–700 nm, CuBHT CE displayed a ~30% increase in the EQE% compared to the device incorporating conventional Pt CE. This improvement can be attributed to the uniform, densely packed morphology of the CuBHT film, which offers high electron transfer pathways and a higher density of catalytically active sites for triiodide/iodide redox reaction to occur. The maximum current density obtained from the EQE spectra of CuBHT and Pt CEs is found to be 9.7 and 7.2 mA cm^{-2}, exhibiting a percentage increase of ~35%. J_{SC} values obtained from EQE measurements are much lower than those observed in J–V curves (Table 1), while the percentage increase (~35%) is much higher despite almost comparable values of J_{SC} (~12 mA cm^{-2}) obtained from the J–V curves. This could be attributed to the recombination processes involved during J–V measurements, which are not considered in EQE measurements. Some other factors for this anomaly include different AM 1.5 photon flux spectrum conditions (standard spectral irradiance in EQE, *c.f.* Xe lamp

Table 1 Measured PV performances of the fabricated DSSCS using Pt-free CuBHT films and Pt CE as reference

CE	J_{SC} (mA cm^{-2})	V_{OC} (V)	FF	PCE (%)
CuBHT	12.11	0.74	0.69	6.27 ± 0.02
Pt	11.59	0.74	0.69	5.99 ± 0.01

© 2026 The Author(s). Published by the Royal Society of Chemistry

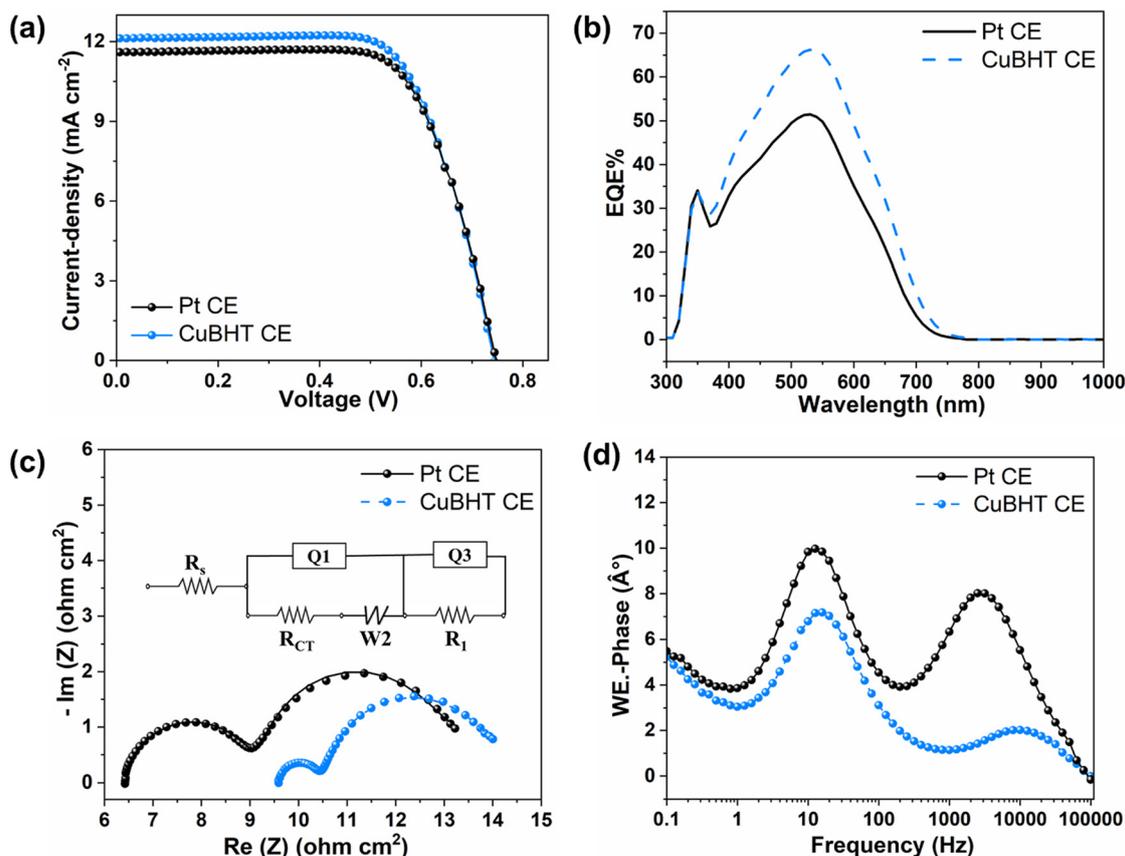*RSC Appl. Interfaces*, 2026, **3**, 420–430 | **427**

Fig. 6 (a) J–V curves of fabricated DSSC devices using Pt counter electrode (reference) and CuBHT MOF film, (b) EQE spectra of CuBHT and Pt CE, (c) Nyquist plots of DSSCs based on CuBHT and Pt CE with the fitted equivalent circuit, and (d) Bode plots of DSSCs fabricated with CuBHT MOF and Pt CE.

in solar simulator for J–V measurements), variation in area of illumination contributing to different photogenerated electrons, more electrolyte degradation in case of EQE due to prolonged illumination, etc.[11,47,48]

Mechanistic understanding of charge transfer through electrochemical impedance spectroscopy (EIS)

To understand the charge transfer dynamics at different interfaces in a DSSC, the EIS technique is employed. EIS measurements were conducted for the device with CuBHT CE with respect to the conventional Pt CE, both fabricated under similar experimental conditions. A typical EIS curve for a DSSC consists of two semicircles corresponding to two key interfaces: the first high-frequency semicircle representing the charge transfer resistance at the counter electrode/electrolyte interface (R_{CT}), and the second lower-frequency

semicircle corresponding to the charge transfer resistance at the photoanode/electrolyte interface (R_1). The contact/series resistance (R_S), which represents the contact resistance from various device components, is obtained from the x-intercept of the first high-frequency semicircle. Fig. 6(c) and Table 2 show the Nyquist plots and EIS parameters of CuBHT and Pt DSSCs, respectively. The inset in Fig. 6(c) shows an equivalent circuit model, $R_S + Q_1(R_{CT} + W) + Q_3/R_1$, used for fitting the experimental data, where R_S is the series resistance, R_{CT} is the charge transfer resistance at the CE/electrolyte interface, R_1 is the charge transfer resistance at the photoanode/ electrolyte interface, Q_1 and Q_3 are the constant phase elements, and W is the Warburg impedance for diffusion-related processes.

It is evident that the R_{CT} for CuBHT CE is dramatically reduced ($R_{CT} = 0.8\ \Omega\ cm^2$) by ~70% compared to that of Pt ($R_{CT} = 2.6\ \Omega\ cm^2$). The higher conductivity and a homogenous, densely packed structure of CuBHT thin film provide a smoother conduction pathway for the electron charge to be transferred from the CE to the electrolyte, leading to a significant reduction in the charge transfer resistance across this interface. In addition, the charge transfer resistance at the photoanode/electrolyte interface is also reduced from $4.2\ \Omega\ cm^2$ to $3.6\ \Omega\ cm^2$ in the case of

Table 2 EIS parameters for the fabricated DSSCs using Pt-free CuBHT films and Pt CE as reference

CE	R_S ($\Omega\ cm^2$)	R_{CT} ($\Omega\ cm^2$)	R_1 ($\Omega\ cm^2$)
CuBHT	9.5	0.8	3.6
Pt	6.4	2.6	4.2

428 | RSC Appl. Interfaces, 2026, **3**, 420–430

© 2026 The Author(s). Published by the Royal Society of Chemistry

CuBHT CE compared to Pt CE. This indicates faster movement of photogenerated electrons, which can be attributed to the catalytic efficiency of CuBHT MOF in the CuBHT-based DSSC. Subsequently, the N719 dye molecules also undergo quick regeneration, preventing recombination of electrons and faster transfer of electron charge to the counter electrode. While the inherent porosity of CuBHT may lead to a marginal increase in series resistance, this is well balanced by the improved interfacial charge dynamics, ultimately resulting in power conversion efficiencies that are comparable to those of conventional Pt-based CEs. Further information on photogenerated electron lifetime at the CE/electrolyte interface of CuBHT CE with respect to Pt CE was obtained from the Bode plots (Fig. 6(d)). The Bode plot exhibits two distinct peaks at low and high frequencies, corresponding to the photoanode/electrolyte and CE/electrolyte interfaces, respectively. The values are summarized in Table 2. Predictably, no shift in the low-frequency peak of CuBHT DSSC compared to Pt DSSC is observed, suggesting a negligible change in the photogenerated electron lifetime at the photoanode/electrolyte interface. These results are in corroboration with the PV performance of the electrocatalytic action of the respective counter electrodes.

Conclusions

In this work, we demonstrate the successful integration of pristine CuBHT as a platinum-free counter electrode in DSSCs. Unlike previous studies that rely on MOF-derived materials, we utilize CuBHT as-is, leveraging its intrinsic π–d conjugation, crystallinity, and electronic conductivity. Interfacial liquid–liquid reaction between copper ions and BHT ligand was used to fabricate CuBHT film on FTO substrate to be incorporated in DSSCs. The resulting devices show promising photovoltaic performance, with the best-performing configuration exhibiting efficient charge transport and low charge-transfer resistance, and catalytic activity towards both I_3^-/I^- and I_2/I^-, similar to Pt. Beyond its high performance, the cost-effectiveness of pristine CuBHT is a key advantage since its synthesis avoids expensive noble metals, high-temperature processing, and multi-step post-synthetic modifications, making it scalable for fabrication. These findings highlight the untapped potential of conductive MOFs as affordable and efficient alternatives to noble metals in photovoltaic devices, and open new avenues for their direct, low-cost application in electrochemical energy systems.

Author contributions

A. G.: writing – original draft, methodology, investigation, formal analysis, data curation, conceptualization. N. K.: validation, methodology, formal analysis, data curation. C.-Y. L.: writing – review & editing, validation, supervision, resources, project administration, methodology, investigation, funding acquisition, conceptualization. D. R.: writing – review & editing, validation, supervision, resources, project administration, methodology, funding acquisition, conceptualization.

Conflicts of interest

There are no conflicts to declare.

Data availability

The data will be made available upon request to the corresponding author.

Supplementary information (SI): the SI includes UV/vis transmittance, photographs showing the progress of bulk CuBHT MOF powder formation, XPS narrow scans of the CuBHT bulk powder, XRF spectrum, Table of DSSC device standardization and their corresponding *J–V* curves, Nyquist plots, Bode plots, and equation for EQE. See DOI: https://doi.org/10.1039/d5lf00311c.

Acknowledgements

Notes and references

1 R. Sasikumar, S. Thirumalaisamy, B. Kim and B. Hwang, *Renewable Sustainable Energy Rev.*, 2024, **199**, 114549.
2 B. O'Regan and M. Grätzel, *Nature*, 1991, **353**, 737–740.
3 Y. Zhang, T. Higashino, K. Namikawa, W. R. Osterloh and H. Imahori, *Chem. Sci.*, 2025, **16**, 15004–15014.
4 F. A. Faraghally, A. F. Musa, C.-C. Chen, Y.-H. Chen, Y.-D. Chen, C.-Y. Yeh and T.-C. Wei, *Small Struct.*, 2024, **5**, 2400236.
5 R. Yao, T. Tan, S. Xu, J. Bai, Z. Gao, B. Mi and W. Huang, *J. Mater. Chem. C*, 2025, **13**, 16232–16241.
6 M. Giordano, F. Cardano, C. Barolo, G. Viscardi and A. Fin, *Adv. Funct. Mater.*, 2025, **35**, 2411230.
7 I. M. Abdellah, *RSC Adv.*, 2025, **15**, 9763–9786.
8 C.-Y. Hsu, H. N. K. Al-Salman, Z. H. Mahmoud, R. M. Ahmed and A. F. Dawood, *Sci. Rep.*, 2024, **14**, 4931.
9 W. Liao, D. Zheng, J. Tian and Z. Lin, *J. Mater. Chem. A*, 2015, **3**, 23360–23367.
10 M. N. Mustafa, S. Shafie, M. H. Wahid and Y. Sulaiman, *Sci. Rep.*, 2019, **9**, 14952.
11 N. Kaur, J. Carrier, M. Vuong, S. Gasso, C.-Y. Lai and D. Radu, *Chem. Eng. J.*, 2025, **516**, 164271.

12 J. Biney, M. Madou, G. Jabbour and J. Park, *ACS Appl. Mater. Interfaces*, 2025, **17**, 17855–17880.

13 S. Rafique, I. Rashid and R. Sharif, *Sci. Rep.*, 2021, **11**, 14830.

14 J. Zhang, J. Li, T. Liang, K. Gan and G. Nong, *ACS Appl. Energy Mater.*, 2024, **7**, 9930–9938.

15 L. H. Kharboot, N. A. Fadil, T. A. A. Bakar, A. S. M. Najib, N. H. Nordin and H. Ghazali, *Materials*, 2023, **16**, 2881.

16 A. H. Alami, B. Rajab, J. Abed, M. Faraj, A. A. Hawili and H. Alawadhi, *Energy*, 2019, **174**, 526–533.

17 K. Gunasekaran, S. Kamesh, N. Wakiya and J. Archana, *Sol. Energy*, 2025, **286**, 113124.

18 L. Fagiolari, E. Varaia, N. Mariotti, M. Bonomo, C. Barolo and F. Bella, *Adv. Sustainable Syst.*, 2021, **5**, 2100025.

19 Y. Zhang, S. E. H. Gilani, M. H. Rasheed, A. Ishaq, F. Saeed, M. Younas, Y. Q. Gill, H. Waheed, A. Shakeel and U. Mehmood, *J. Power Sources*, 2025, **652**, 237641.

20 A. Dhakshinamoorthy, Z. Li, S. Yang and H. Garcia, *Chem. Soc. Rev.*, 2024, **53**, 3002–3035.

21 W. Wang, D. Chen, F. Li, X. Xiao and Q. Xu, *Chem*, 2024, **10**, 86–133.

22 H.-C. J. Zhou and S. Kitagawa, *Chem. Soc. Rev.*, 2014, **43**, 5415–5418.

23 O. M. Yaghi, M. O'Keeffe, N. W. Ockwig, H. K. Chae, M. Eddaoudi and J. Kim, *Nature*, 2003, **423**, 705–714.

24 H. Furukawa, K. E. Cordova, M. O'Keeffe and O. M. Yaghi, *Science*, 2013, **341**, 1230444.

25 C. Nizamudeen, R. Krishnapriya, M. S. Mozumder, A. H. I. Mourad and T. Ramachandran, *Sci. Rep.*, 2023, **13**, 6345.

26 R. Krishnapriya, C. Nizamudeen, B. Saini, M. S. Mozumder, R. K. Sharma and A. H. I. Mourad, *Sci. Rep.*, 2021, **11**, 16265.

27 S.-H. Hsu, C.-T. Li, H.-T. Chien, R. R. Salunkhe, N. Suzuki, Y. Yamauchi, K.-C. Ho and K. C. W. Wu, *Sci. Rep.*, 2014, **4**, 6983.

28 J. Ou, J. Xiang, J. Liu and L. Sun, *ACS Appl. Mater. Interfaces*, 2019, **11**, 14862–14870.

29 W. Moloto, P. Mbule, E. Nxumalo and B. Ntsendwana, *Sci. Rep.*, 2024, **14**, 11292.

30 J. Ho Kim, H. Woo Park, S.-J. Koo, D. Lee, E. Cho, Y.-K. Kim, M. Shin, J. Woo Choi, H. Jung Lee and M. Song, *J. Energy Chem.*, 2022, **67**, 458–466.

31 H. T. B. Pham, J. Y. Choi, M. Stodolka and J. Park, *Acc. Chem. Res.*, 2024, **57**, 580–589.

32 H. Meng, Y. Han, C. Zhou, Q. Jiang, X. Shi, C. Zhan and R. Zhang, *Small Methods*, 2020, **4**, 2000396.

33 X. Huang, P. Sheng, Z. Tu, F. Zhang, J. Wang, H. Geng, Y. Zou, C.-a. Di, Y. Yi, Y. Sun, W. Xu and D. Zhu, *Nat. Commun.*, 2015, **6**, 7408.

34 C. Meng, P. Hu, H. Chen, Y. Cai, H. Zhou, Z. Jiang, X. Zhu, Z. Liu, C. Wang and A. Yuan, *Nanoscale*, 2021, **13**, 7751–7760.

35 F. Li, X. Zhang, X. Liu and M. Zhao, *ACS Appl. Mater. Interfaces*, 2018, **10**, 15012–15020.

36 X. Chen, Y. Lu, J. Dong, L. Ma, Z. Yi, Y. Wang, L. Wang, S. Wang, Y. Zhao, J. Huang and Y. Liu, *ACS Appl. Mater. Interfaces*, 2020, **12**, 57235–57244.

37 X. Chen, J. Dong, K. Chi, L. Wang, F. Xiao, S. Wang, Y. Zhao and Y. Liu, *Adv. Funct. Mater.*, 2021, **31**, 2102855.

38 X. Huang, H. Yao, Y. Cui, W. Hao, J. Zhu, W. Xu and D. Zhu, *ACS Appl. Mater. Interfaces*, 2017, **9**, 40752–40759.

39 Z. Jin, J. Yan, X. Huang, W. Xu, S. Yang, D. Zhu and J. Wang, *Nano Energy*, 2017, **40**, 376–381.

40 Y. Wu, Y. Luo, P. K. Chu and C. Menon, *Nano Energy*, 2023, **111**, 108427.

41 C.-Y. Chang, N. Kaur, R. Prado-Rivera, C.-Y. Lai and D. Radu, *ACS Appl. Mater. Interfaces*, 2024, **16**, 13719–13728.

42 N. Kaur, L. Biswal, A. Prieto, C.-Y. Lai and D. R. Radu, *ACS Appl. Energy Mater.*, 2024, **7**, 5038–5049.

43 Z. Pan, X. Huang, Y. Fan, S. Wang, Y. Liu, X. Cong, T. Zhang, S. Qi, Y. Xing, Y.-Q. Zheng, J. Li, X. Zhang, W. Xu, L. Sun, J. Wang and J.-H. Dou, *Nat. Commun.*, 2024, **15**, 9342.

44 A. Bétard and R. A. Fischer, *Chem. Rev.*, 2012, **112**, 1055–1083.

45 M. de Lourdes Gonzalez-Juarez, C. Morales, J. I. Flege, E. Flores, M. Martin-Gonzalez, I. Nandhakumar and D. Bradshaw, *ACS Appl. Mater. Interfaces*, 2022, **14**, 12404–12411.

46 C. Singh, C. B. Jha, A. S. Anand, E. Kohli, N. Manav, R. Varshney, S. Upadhyayula and R. Mathur, *ACS Appl. Bio Mater.*, 2025, **8**, 2440–2458.

47 M. Saliba, E. Unger, L. Etgar, J. Luo and T. J. Jacobsson, *Nat. Commun.*, 2023, **14**, 5445.

48 Q. Yang, K. Bittkau, A. Eberst, U. Rau and K. Ding, *Sol. Energy Mater. Sol. Cells*, 2024, **273**, 112953.